Dual-Zone Material Assignment Method for Correcting Partial Volume Effects in Image-Based Bone Models

Brendan Inglis, MSa, Daniel Grumbles, MSa, and Hannah L. Dailey, PhDa*

 a Department of Mechanical Engineering and Mechanics, Lehigh University, Bethlehem, PA, USA

Corresponding Author:

Hannah Dailey, PhD 19 Memorial Drive West Packard Lab Room 356 Bethlehem, PA 18015 USA Tel: +1 (610) 758-4112

Tel: +1 (610) 758-4112 hannah.dailey@lehigh.edu **Dual-Zone Material Assignment Method for Correcting Partial Volume Effects in Image-Based Bone Models**

Abstract

In image-based finite element analysis of bone, partial volume effects (PVEs) arise from image blur at tissue boundaries and as a byproduct of geometric reconstruction and meshing during model creation. In this study, we developed and validated a material assignment approach to mitigate partial volume effects. Our validation data consisted of physical torsion testing of intact tibiae from N = 20 Swiss alpine sheep. We created finite element models from micro-CT scans of these tibiae using three popular element types (10-node tetrahedral, 8-node hexahedral, and 20-node hexahedral). Without partial volume management, the models over-predicted the torsional rigidity compared to physical biomechanical tests. To address this problem, we implemented a dual-zone material model to treat elements that overlap low-density surface voxels as soft tissue rather than bone. After in situ inverse optimization, the dual-zone material model produced strong correlations and high absolute agreement between the virtual and physical tests. This suggests that with appropriate partial volume management, virtual mechanical testing can be a reliable surrogate for physical biomechanical testing. For maximum flexibility in partial volume management regardless of element type, we recommend the use of the following dual-zone material model for ovine tibiae: soft-tissue cutoff density of 665 mgHA/cm³ with a soft tissue modulus of 50 MPa (below cutoff) and a density-modulus conversion slope of 10,225 MPa-cm³/mgHA for bone (above cutoff).

Keywords: finite element analysis; computed tomography; cortical bone; virtual mechanical testing

Introduction

Partial volume effects (PVEs) are a known byproduct of medical imaging and image-based finite element analysis (FEA). Partial volume effects first arise at the image-acquisition stage. In computed tomography (CT) imaging, when tissues of widely different absorption are captured within the same CT voxel, they produce an effective local X-ray attenuation (Hounsfield Unit [HU]) that is proportional to the weighted average value for the tissues within the volume (Keyak et al. 1990; Merz et al. 1996; Cattaneo et al. 2001; Taddei et al. 2004). These partial volume effects appear as image "blur" at tissue boundaries, such as between mineralized and non-mineralized tissue (Falcinelli et al. 2016) and when resolving thin features in cortical bone (Pakdel et al. 2012). The blur creates a halo effect that thickens the apparent cortical geometry (Rittweger et al. 2004). These effects can be mitigated by acquiring images with smaller voxels, but they are inevitable. Image-acquisition PVEs can be mitigated through image deblurring using a deconvolution filter by estimating the point spread function of the acquired image, computing its inverse, and convolving the acquired image with that inverse (Pakdel et al. 2014; Pakdel et al. 2016).

In image-based finite element models of bone, partial volume effects introduce challenges for inferring bone material properties. For example, the Young's modulus is known to be proportional to the radiodensity (bone mineral density). Numerous density-modulus scaling functions can be chosen from the literature based on the species and anatomic site being considered (Helgason, Perilli, et al. 2008; Knowles et al. 2016). However, at the blurred bone boundaries, partial volume effects create voxels that appear to be lower in density, and therefore lower in effective modulus, than the actual bone. PVEs can cause errors in surface material property mapping for elementwise material assignment in FE models, which can cause particular

challenges for estimating strain at cortical surfaces and in thin structures (Falcinelli et al. 2016; Falcinelli and Whyne 2020; Schileo et al. 2020). One technique for correcting this is node-based material property assignment, but this method is not always straightforward to implement depending on the FE analysis package being used (Helgason, Taddei, et al. 2008). Other methods include the cortical bone mapping (CBM) technique, and model-based and machine learning-based approaches, which have been recently reviewed (Falcinelli and Whyne 2020).

Partial volume effects also arise in finite element model geometry reconstruction and meshing. Any time the geometry of an element is not perfectly aligned with the underlying voxels, the tissue composition and material properties of that element must be inferred by mapping from multiple radiodensity values in neighboring voxels (Fig. 1). Depending on the conformation of the element and morphometry of the scanned tissues, this mapping process can result in an under- or overestimation of the elemental stiffness relative to the physiologic properties for the tissues at that region of space (Poelert et al. 2013). Partial volume effects are a challenge in image-based finite element modeling because if not appropriately managed, they can lead to systematic errors in model results (Peleg et al. 2014; Schileo et al. 2020).

One potential solution to the problem of reconstruction partial volume effects is to build voxel-based hexahedral meshes. In this approach, each voxel directly becomes an element and its local material assignment depends on only the radiodensity of that voxel (Fig. 1). This approach is attractive for its simplicity, but it has several possible limitations that need to be explored. First, in high-resolution micro-CT imaging, the number of voxels may be too large for tractable finite element model creation, so a down-sampling procedure may be required (Cattaneo et al. 2001). This could enhance the boundary-blurring effect of partial volumes in the underlying image. Second, voxel-based hexahedral meshes do not follow the curved boundaries of the bone

tissue itself, so they sacrifice some physiologic geometric accuracy that may be more easily preserved using tetrahedral elements (Cattaneo et al. 2001). Finally, both hexahedral and tetrahedral meshes may be sensitive to thresholding effects in image segmentation, a process that determines which voxel volumes are to be included in the model as bone tissue and which are to be ignored.

Accordingly, the objective of this study was to explore the potential utility of a material-assignment solution to the issue of partial volumes in bone finite element models, considering both the image-acquisition and model-reconstruction effects. We hypothesized that a piecewise material assignment law can serve as a correcting factor to be applied after meshing as a strategy for partial volume management. We sought to identify a density threshold above which elements are to be treated as bone, and below which they are to be considered as soft tissue. We used *in situ* inverse optimization to identify a piecewise material assignment law that produced best agreement between model-predicted torsional rigidity of intact ovine tibiae and the results of physical bench tests of the same specimens.

Materials and Methods

An overview of the study design is presented in Fig. 2.

Animal Study Information

As part of a previously completed *in vivo* study, 20 intact tibiae were harvested from adult female Swiss alpine sheep (2-3 years old, weight 59-87 kg). The details of these experiments have been previously reported (Schwarzenberg et al. 2021). All animal experiments were approved by the local governmental authorities of the canton of Zurich, Switzerland and

conducted according to the Swiss laws of animal protection and welfare and approved by the local governmental veterinary authorities (license numbers ZH071/17 and ZH183/17).

Imaging and Mechanical Testing

After sacrifice, the tibiae were dissected and soft tissue removed. Micro-computed tomography (μ CT) scans of the diaphyseal segments were performed using an XtremeCT II Micro-CT scanner (Scanco Medical AG) with an X-ray voltage of 68 kVp and X-ray current of 1,470 μ A with a resulting isotropic scan resolution of 60.7 μ m. A phantom was scanned with the same settings (Scanco KP70 phantom, QRM) to convert from Hounsfield Units [HU] to calibrated radiodensity, ρ_{QCT} [mgHA/cm³]. All samples were tested in a custom-made fixture using an Instron E10000 electrodynamic testing machine. Axial loading and torque were measured with a calibrated load cell (± 10 kN/ ± 100 N-m). An axial preload of 5 N was maintained throughout the test. An internal rotation of 5° per minute was then applied. Biomechanical torsional rigidity (GJ) was calculated by multiplying the slope from a linear regression of the torque-angle loading curve between 6 and 10 N-m by the specimen gauge length.

Scan Processing and Model Creation

The μCT scans were processed using Materialize Mimics (21.0, Plymouth, MI). To align the primary axis of the tibiae with the coordinate axes, the models were realigned and resliced. All μCT scans were down-sampled to an isotropic resolution of 400 μm, which is comparable to clinical-resolution scanning. The resulting image stacks were used for building image-based finite element models. A threshold mask of 400-4,000 Hounsfield Units (HU) was applied to all models, which encapsulates the full phantom density range in the ovine tibiae (Schwarzenberg et al. 2021). The mask volumes completely encapsulated the cortical bone and the regions of

boundary blurring due to partial volume effects at the periosteal and endosteal bone surfaces.

The medullary void spaces were not included in the models.

Virtual Mechanical Testing

Each of the 20 individual bone models were meshed using linear hexahedral (Hex-8), quadratic hexahedral (Hex-20), and quadratic tetrahedral (Tet-10) elements. The Hex-8 meshes were created using the Mimics built-in "Create Voxel Mesh" tool, using a uniform voxel mesh of 0.4 mm. Filtering for small parts was enabled to remove any unconnected bodies. The Hex-20 meshes were created by editing the Hex-8 meshes from Mimics using HyperMesh (2021.2, Troy, MI) and adding mid-side nodes to each element to convert from linear elements to quadratic. To create the Tet-10 meshes, the mask was smoothed and wrapped within Mimics, then exported to 3Matic (15.0, Plymouth, MI), where a 1 mm quadratic tetrahedral mesh was applied. Material properties were applied in each mesh using the techniques discussed in the *Elementwise Material Property Assignment* section below.

Finite element meshes with material properties were imported into ANSYS (2020 R2, Canonsburg, PA) and subjected to virtual torsion testing for comparison to the postmortem biomechanical torsional rigidity data for each animal (Fig. 2). Procedures for virtual torsion testing were developed in a previous study (Schwarzenberg et al. 2019). In ANSYS, the distal end of each tibia was fixed in translation and rotation and the proximal end was rotated by one degree about the long axis of the bone, leaving all other degrees of freedom unfixed. For each model, virtual torsional rigidity was then calculated as follows:

$$VTR = \frac{ML}{\phi} \tag{1}$$

where M is the calculated moment reaction, L is the working length of the test segment, and ϕ is the applied angle of twist. Torsional rigidity was assessed, rather than torsional stiffness, because it eliminates the effects of varying specimen gage length across the cohort.

Mesh Convergence

A mesh convergence study was performed on a representative model to determine appropriate mesh sizes for quadratic tetrahedral (Tet-10) and linear hexahedral (Hex-8) elements. The results from the Hex-8 convergence study were used as a basis for Hex-20 mesh sizing because quadratic hexahedral (Hex-20) elements converge faster than linear hexahedral (Hex-8) elements (Moaveni 2007; Huei Huang Lie 2021). Linear tetrahedral elements were not tested, as previous research indicates their slower convergence behavior and lower accuracy for curved surfaces compared to higher-order tetrahedral elements (Viceconti et al. 1998; Moaveni 2007; Chen et al. 2010; Huei Huang Lie 2021). The convergence criteria used for the Tet-10 models was a percentage change in VTR less than 1%. The Tet-10 models achieved convergence with a uniform maximum edge length of 1 mm for surfaces and volumes. The Hex-8 elements achieved convergence with a percent change in VTR less than 2% isotropic sizes of 1.0 mm or less. However, direct mapping from voxels to finite elements has procedural advantages for highthroughput modeling and avoidance of reconstruction partial volume affects. Accordingly, both the Hex-8 and Hex-20 models were run with uniform isotropic element sizes of 0.4 mm, which is a clinically realistic voxel/element size value below their demonstrated convergence limit. Additional details of the mesh convergence analysis are included in the Supplemental Digital Content.

Elementwise Material Property Assignment

Material properties for each mesh type (Tet-10, Hex-8, and Hex-20) were assigned in Mimics and exported. A custom MATLAB (R2020b, Natick, MA) function was used to assign material properties to elements based on the underlying voxel grayscale value reported in HU, which was converted to radiodensity [mgHA/cm³] using a radiological phantom. The brighter the voxel, the higher the bone mineral density of the tissue.

The piecewise material model for managing partial volume effects was defined with two regions separated by a density cutoff, ρ_{cut} . Elements with effective densities above ρ_{cut} were treated as cortical bone with material properties defined as a generalized zero-intercept linear function, following the form identified in our previous study (Schwarzenberg et al. 2021). Elements with effective densities below ρ_{cut} were treated as unmineralized soft tissue with a constant elastic modulus, E_s . The resulting piecewise material model can be represented as follows:

$$E_{i} = \begin{cases} E_{s} & \rho_{QCT,i} < \rho_{cut} \\ \alpha \times \rho_{QCT,i} & \rho_{QCT,i} \ge \rho_{cut} \end{cases}$$
 (2)

where E_i is the local Young's modulus [MPa] of the i^{th} finite element and $\rho_{QCT,i}$ is that element's effective phantom-calibrated radiodensity [mgHA/cm³]. The soft tissue modulus value (E_s) was fixed at 50 MPa, based on a previous study of healing ovine tibiae with fracture callus (Inglis et al. 2022) and the results of a sensitivity study (see Supplemental Digital Content). A Poisson's ratio of 0.3 was assumed for all elements (Wirtz et al. 2000; Simon et al. 2011).

Response Surface Optimization

The material model parameters α and ρ_{cut} were fit using a response surface optimization. An initial design space was chosen using seven equally spaced points for both slope (α = 5,000-20,000 MPa-cm³/mgHA) and density cutoff (ρ_{QCT} = 0-1,500 mgHA/cm³). The range of slopes was chosen to encapsulate a range of literature values for density-modulus scaling relations (Helgason, Perilli, et al. 2008; Knowles et al. 2016; Schwarzenberg et al. 2021), and the range of density cutoffs was chosen to encapsulate the full density range of the ovine scans (Inglis et al. 2022). At each design point, the root mean squared error (RMSE) was calculated for the difference between the virtual torsion tests (VTR values) and physical biomechanical tests (GJ values). After an initial round of analysis, the response surface was refined around regions of interest with the lowest RMSE values using an additional three slopes and nine cutoffs, to determine if a new global minimum could be found.

As previously reported, the postmortem biomechanical testing of these specimens produced a group torsional rigidity of GJ = 1.180 ± 0.187 N-m²/° (Schwarzenberg et al. 2021). Throughout the results, this dataset is referred to as the "Bio" group. This data was used as the target for optimization of the dual-zone material models for partial-volume management. It was also used to define an *a priori* acceptance criterion for model validity. For a reliable virtual mechanical test, we required RMSE values for the comparison between virtual and physical tests to be less than the standard deviation (SD) of the Bio group (SD = 0.187). This RMSE criterion produces a plane on the response surface; any design points below the plane represent combinations of slopes (α) and cutoffs (ρ_{cut}) in the dual-zone material model that produce valid virtual torsion tests. All design points that meet the validity requirement are described as lying in the "trough of acceptability" for the response surface (see Fig. 2D).

Data Processing, Visualization, and Statistical Analysis

Virtual mechanical testing post-processing was performed in MATLAB. The mesh data, the material model data, and the mechanical testing results from ANSYS were queried using custom MATLAB functions. Contour slice plots and 3D visualizations of models and results were generated using Paraview (5.9.0, Sandia National Laboratories, Kitware Inc, Los Alamos National Laboratory).

Descriptive statistics were generated in Microsoft Excel (Office 365; Redmond, WA). Statistical analyses were generated using IBM SPSS Statistics 27 (Armonk, NY). Pearson's correlations were used to determine the strength of association between the virtual and biomechanical torsional rigidity datasets. A correlation coefficient $R \ge 0.8$ ($R^2 \ge 0.64$) was defined as strong and $R \ge 0.6$ ($R^2 \ge 0.36$) was defined as moderate (Akoglu 2018). One-way repeated-measures ANOVA was performed to determine if there were statistically significant differences between the measured torsional rigidity from biomechanical testing (GJ) and predicted VTR in the optimized material models for each of the three element types (Tet-10, Hex-8, Hex-20 for combinations of E_s and ρ_{cut}). Post hoc analysis with a Bonferroni adjustment was performed on pairwise comparisons to identify statistically significant differences. All values reported are averages and standard deviations unless otherwise stated. The statistical significance limit was p = 0.05.

Results

Simulations were performed on every combination of slope and cutoff for each animal and element type. In total, 9,600 simulations were run in parallel using Lehigh's High-Performance Computing (HPC) server to construct response surfaces using all N=20 tibiae for each of the three element

types (Tet-10, Hex-8, and Hex-20). This process successfully identified the optimized combination of dual-zone material model slope (α) and soft tissue cutoff (ρ_{cut}) that produced the best agreement between the torsional rigidity values from postmortem torsion testing (GJ) and model-predicted virtual torsional rigidity (VTR) in all specimens. Representative results for the Hex-20 element type are shown in Fig. 3. In the non-optimized material models, selecting higher slope values led to higher VTR values. Increasing the density cutoff was generally associated with decreasing VTR due to the increasing number of elements being treated as soft tissue in the finite element model. The zero cutoff case was included to represent a linear density-modulus scaling function with no partial-volume management.

Without the dual-zone material model ($\rho_{cut}=0$), the best-fit linear material assignment produced a strong and significant correlation between VTR and GJ ($R^2=0.692$, p<0.005), with a small but systematic over-prediction of torsional rigidity with RMSE = 0.246 (Fig. 4A). This case did not meet our pre-defined acceptance criteria of RMSE less than the datum SD (RMSE = 0.246 > SD = 0.187). Increasing the cutoff steadily decreased the predicted VTR values. At the optimal design point (minimum RMSE; Fig. 3B), the correlation between GJ and VTR was strong and significant ($R^2=0.729$, p<0.005), with good absolute agreement between the physical and virtual tests (Fig. 4B). The optimal design point met our pre-defined acceptance criteria for model validity (RMSE = 0.099 < datum SD = 0.187). Overshooting the ideal density cutoff led to a dramatic reduction in predicted torsional rigidity and large RMSE (Fig. 4C), with too many elements being assigned modulus values for soft tissue.

Repeating this process with each element type (Tet-10, Hex-8, Hex-20) showed that all three model types were capable of achieving good agreement between GJ and VTR (Fig. 5). GJ and VTR values at these optimal design points were normally distributed according to the Shapiro-

Wilk test for normality (all p > 0.05). ANOVA showed that among the optimized groups, model type was not a significant factor (all p > 0.05) and that there were no significant differences relative to the Bio group (all p > 0.05).

The results also showed that the minimum RMSE design points identified in Fig. 5 are not unique in their ability to meet the pre-defined acceptance criteria for model validity. The response surfaces for each element type revealed a range of combinations of slope (α) and soft tissue cutoff (ρ_{cut}) that produce RMSE values below the datum standard deviation (Fig. 6). Within the resulting "trough of acceptability" on the response surface, the values of slope and cutoff that strictly minimized RMSE were considered the optimal design points (red dots in Fig. 6). Table 1 displays the optimal design points for each element type as well as the extremes of the design space (minimum slope with minimum cutoff and maximum slope with maximum cutoff). An additional design point between the optimal and the maximum design points was included in Table 1 to demonstrate the weak correlation coefficients between GJ and VTR that are produced when the cutoff is raised past the optimum. Further increasing the density cutoff leads to increasing R^2 values but increasing RMSE (worse agreement between GJ and VTR). This effect arises due to the relative homogeneity of the cortical bone, with variations between specimens reflecting largely geometric effects such as cortical wall thickness.

Discussion

This study confirmed both the reliability and flexibility of virtual mechanical testing as a surrogate for postmortem torsion testing of intact cortical bone segments in a large animal model. All three choices of element types (Tet-10, Hex-8, and Hex-20) were capable of reliably recapitulating the physical bench test, based on our *a priori* acceptance criteria of RMSE < datum SD. The performance of all three element types was similar with respect to virtual

torsional rigidity. This suggests that investigators have some freedom to choose the element type that is most expedient for their modeling workflow and software availability.

The dual-zone material modeling approach was also successful in managing model-reconstruction partial volume effects, although there were some differences in implementation based on element type. The simplest option for building image-based finite element models would be a direct voxel-based hexahedral mesh. When size-matched to the voxels at image acquisition, hexahedral elements have no reconstruction partial volume effects, only the inevitable image-acquisition partial volume effects (Fig. 1). However, high-resolution micro-CT imaging may produce excessively large direct voxel-based meshes, necessitating some down-sampling of images before meshing. The dual-zone material model successfully corrected for the partial volume effects at the cortical surfaces in our down-sampled Hex-8 and Hex-20 meshes, although the optimal design point (minimum RMSE) was slightly different for these element types. As expected, the optimal slope α was slightly lower for Hex-8 elements than Hex-20 elements, which we attribute to the inherent stiffer behavior of linear finite elements compared to quadratic elements.

The Tet-10 element behavior with the dual-zone model was also different compared to the Hex-8 and Hex-20 elements, most notably in the density cutoff identified from the response surface optimization. For the tetrahedral elements, the optimal cutoff was lower (ρ_{cut} = 750 mgHA/cm³) compared to the cutoffs for the hexahedral elements (ρ_{cut} = 1050 and 1100 mgHA/cm³), see Fig. 5. This effect is explained by the relatively larger surface element sizes in the tetrahedral meshes compared to hexahedral meshes. Tetrahedral meshes produce larger numbers of elements compared hexahedral elements when meshing the same volumes (Table 2), so the element sizes that produced mesh convergence had larger edge lengths with the Tet-10

mesh compared to the Hex-8 and Hex-20 elements. The dual-zone material model applies soft-tissue material properties to elements with voxel-averaged densities below the cutoff. For our meshes, this meant that surface tetrahedra added to the "soft tissue" group had greater depth of penetration into the cortical wall than surface hexahedra did. The lower cutoff produced in the dual-zone material model for Tet-10 elements was the result of this geometric effect and helped to avoid over-correction and under-prediction of VTR with this element type. The correlation coefficients and RMSEs were in close agreement across all element types.

For practical implementation of these findings, it would be ideal to identify a single dual-zone material model (combination of α and ρ_{cut}) that can successfully manage partial volume effects and produce valid predictions of tibial torsional rigidity in any element type. Referring to the response surfaces of Fig. 6, such a candidate point would lie within the trough of acceptability for all three element types. For the design points considered here, we identified several combinations of α and ρ_{cut} that satisfy the *a priori* model acceptance criterion for all three tested element types.

To further guide the selection of a unique dual-zone model that can manage partial volume effects for any element type, we considered that the "soft tissue" element category in these models is almost entirely driven by partial volume effects. These tibiae were excised before scanning and had very little periosteal soft tissue. Other applications of virtual mechanical testing may involve considerably more soft tissue. For example, in another recent study, we examined the mechanical contribution of soft tissue within the callus of a healing fracture (Inglis et al. 2022). We optimized a dual-zone material model that was capable of differentiating between mineralized bone and interstitial soft tissues within the callus. The resulting slope and cutoff values for ovine tibiae with fracture callus were $\alpha = 10,225$ MPa-cm³/mgHA and $\rho_{cut} = 665$

mgHA/cm³. When applied to the intact tibiae of this study, this combination of slope and cutoff fell within the trough of acceptability for all three element types (see orange dots in Fig. 6). Accordingly, for maximum flexibility in the use of a dual-zone material model for management of both partial volume effects and soft tissue effects in ovine tibiae with or without fracture callus, we recommend the use of $\alpha = 10,225$ MPa-cm³/mgHA and $\rho_{cut} = 665$ mgHA/cm³ in Eq. 2. For the three element types considered with intact bones here, this design point produced the following goodness-of-fit statistics: Tet-10 (R² = 0.705, RMSE = 0.131), Hex-20 (R² =0.744, RMSE = 0.120), and Hex-20 (R² =0.694, RMSE = 0.127). An interactive and exploratory visualization of this design point and the trough of acceptability can be accessed through a web application that is linked from the Supplemental Digital Content.

Implementation of this approach to partial volume management for virtual mechanical testing in other species and anatomic sites could be pursued one of two ways. When possible, the ideal approach is to perform the *in situ* inverse optimization of the dual-zone material assignment law using image-based finite element models and reference biomechanical testing data. When this is not possible, an existing material assignment law can be leveraged in lieu of the linear function in Eq. 2. We recommend retention of the 50 MPa soft modulus. To identify the density cutpoint in the new species, we recommend scaling $\rho_{cut} = 665 \text{ mgHA/cm}^3$ (ovine tibial cortical bone) to a new ρ_{cut} by comparing the median cortical bone densities across the two species. For reference, the median cortical bone density for all sheep in this study was 1250 mgHA/cm³. A histogram and descriptive statistics of the voxelized ρ_{QCT} values in all scans used in this study has been included in the Supplemental Digital Content.

There are limitations to this study. First, the "soft tissue" stiffness assigned for the dual-zone approach to partial volume management was set to be a constant value (50 MPa) based on

our previous study (Inglis et al. 2022). There is a lack of widespread agreement in the literature on the definitive stiffness or material properties of musculoskeletal soft tissues. The current study was not able to probe these potential variations because the tested specimens had very little soft tissue covering and the predicted torsional rigidity was not sensitive to differences in E_S below 50 MPa. For this reason, the results of this study should not be interpreted as a confirmation of the mechanical properties of soft tissues surrounding the ovine tibiae. An additional limitation to this study is that we only had cortical bone samples and with these, only torsion testing data was available for virtual model validation. These tests were not instrumented for strain acquisition. The results of this study suggest that with appropriate partial volume management, any element type can be used to reliably predict the torsional rigidity of an intact tibia, but there may be other important differences between elements that are not addressed here, such as the representation of surface stress and strain. While the torsion test selected here is the gold-standard test for ovine tibiae, selection of an appropriate validation test remains paramount for the development of new applications in image-based finite element modeling. The dual-zone approach to PVE management may also require additional development for analysis of samples with mixed cortical and trabecular bone, due to the relatively lower density of trabecular zones.

Finally, it is worth noting that the dual-zone material modeling approach for PVE management could be hybridized with other approaches in the literature. For example, deblurring reduces but does not completely eliminate PVEs and their associated errors at cortical boundaries (Falcinelli and Whyne 2020). Node-based material assignment reduces the relative geometric size of PVE errors compared to elementwise material assignment, but still requires the use of an assignment law to estimate local mechanical properties from the voxelized intensity data (Helgason, Taddei, et al. 2008), which could over-estimate the mechanical property assigned at

nodes that fall within the PVE halo. Combining the dual-zone material modeling approach with some of these other techniques may be helpful in further increasing the accuracy of subject-specific finite element modeling for virtual mechanical testing applications in bone.

Acknowledgments

This material is based upon work supported by the National Science Foundation (NSF) under Grant No. CMMI-1943287. The preclinical studies from which this data was obtained were funded by the Johnson & Johnson Family of Companies and Biomech Innovations. The authors wish to thank Beat Lechmann (Johnson & Johnson Family of Companies) and Stefano Brianza (Biomech Innovations AG) for agreeing to grant access to the ovine studies data for our analyses. Portions of this research were conducted on Lehigh University's Research Computing infrastructure partially supported by NSF Award 2019035.

Declaration of Interest Statement

The authors have no conflicts of interest relevant to this work.

References

Akoglu H. 2018. User's guide to correlation coefficients. Turkish J Emerg Med. 18(3):91–93. https://doi.org/10.1016/j.tjem.2018.08.001

Cattaneo PM, Dalstra M, Frich LH. 2001. A three-dimensional finite element model from computed tomography data: A semi-automated method. Proc Inst Mech Eng Part H J Eng Med. 215(2):203–213. https://doi.org/10.1243/0954411011533760

Chen G, Schmutz B, Epari D, Rathnayaka K, Ibrahim S, Schuetz MA, Pearcy MJ. 2010. A new approach for assigning bone material properties from CT images into finite element models. J Biomech [Internet]. 43(5):1011–1015. https://doi.org/10.1016/j.jbiomech.2009.10.040

Falcinelli C, Schileo E, Pakdel A, Whyne C, Cristofolini L, Taddei F. 2016. Can CT image deblurring improve finite element predictions at the proximal femur? J Mech Behav Biomed Mater [Internet]. 63:337–351. https://doi.org/10.1016/j.jmbbm.2016.07.004

Falcinelli C, Whyne C. 2020. Image-based finite-element modeling of the human femur. Comput Methods Biomech Biomed Engin [Internet]. 0(0):1138–1161.

https://doi.org/10.1080/10255842.2020.1789863

Helgason B, Perilli E, Schileo E, Taddei F, Brynjólfsson S, Viceconti M. 2008. Mathematical relationships between bone density and mechanical properties: A literature review. Clin Biomech. 23(2):135–146. https://doi.org/10.1016/j.clinbiomech.2007.08.024

Helgason B, Taddei F, Pálsson H, Schileo E, Cristofolini L, Viceconti M, Brynjólfsson S. 2008. A modified method for assigning material properties to FE models of bones. Med Eng Phys. 30(4):444–453. https://doi.org/10.1016/j.medengphy.2007.05.006

Huei Huang Lie. 2021. Finite Element Simulations with ANSYS Workbench 2021 [Internet]. :617. http://gen.lib.rus.ec/book/index.php?md5=550699FFEB4A7E39926ECA05AD4C4561 Inglis B, Schwarzenberg P, Klein K, von Rechenberg B, Darwiche S, Dailey HL. 2022. Biomechanical duality of fracture healing captured using virtual mechanical testing and validated in ovine bones. Sci Rep [Internet]. 12(1):1–13. https://doi.org/10.1038/s41598-022-06267-8

Keyak JH, Meagher JM, Skinner HB, Mote CD. 1990. Automated three-dimensional finite element modelling of bone: a new method. J Biomed Eng. 12(5):389–397.

https://doi.org/10.1016/0141-5425(90)90022-F

Knowles NK, Reeves JM, Ferreira LM. 2016. Quantitative Computed Tomography (QCT) derived Bone Mineral Density (BMD) in finite element studies: a review of the literature. J Exp Orthop. 3(1). https://doi.org/10.1186/s40634-016-0072-2

Merz B, Niederer P, Müller R, Rüegsegger P. 1996. Automated finite element analysis of excised human femora based on precision-qct. J Biomech Eng. 118(3):387–390. https://doi.org/10.1115/1.2796021

Moaveni S. 2007. Finite Element Analysis Theory and Application with ANSYS [Internet]. [place unknown]. http://www.amazon.com/Finite-Element-Analysis-Application-Edition/dp/0131890808

Pakdel A, Fialkov J, Whyne CM. 2016. High resolution bone material property assignment yields robust subject specific finite element models of complex thin bone structures. J Biomech [Internet]. 49(9):1454–1460. https://doi.org/10.1016/j.jbiomech.2016.03.015

Pakdel A, Mainprize JG, Robert N, Fialkov J, Whyne CM. 2014. Model-based PSF and MTF

estimation and validation from skeletal clinical CT images. Med Phys. 41(1). https://doi.org/10.1118/1.4835515

Pakdel A, Robert N, Fialkov J, Maloul A, Whyne C. 2012. Generalized method for computation of true thickness and x-ray intensity information in highly blurred sub-millimeter bone features in clinical CT images. Phys Med Biol. 57(23):8099–8116. https://doi.org/10.1088/0031-9155/57/23/8099

Peleg E, Herblum R, Beek M, Joskowicz L, Liebergall M, Mosheiff R, Whyne C. 2014. Can a partial volume edge effect reduction algorithm improve the repeatability of subject-specific finite element models of femurs obtained from CT data? Comput Methods Biomech Biomed Engin. 17(3):204–209. https://doi.org/10.1080/10255842.2012.673595

Poelert S, Valstar E, Weinans H, Zadpoor AA. 2013. Patient-specific finite element modeling of bones. Proc Inst Mech Eng Part H J Eng Med. 227(4):464–478.

https://doi.org/10.1177/0954411912467884

Rittweger J, Michaelis I, Giehl M, Wüsecke P, Felsenberg D. 2004. Adjusting for the partial volume effect in cortical bone analyses of pQCT images. J Musculoskelet Neuronal Interact. 4(4):436–441.

Schileo E, Pitocchi J, Falcinelli C, Taddei F. 2020. Cortical bone mapping improves finite element strain prediction accuracy at the proximal femur. Bone [Internet]. 136(March):115348. https://doi.org/10.1016/j.bone.2020.115348

Schwarzenberg P, Klein K, Ferguson SJ, Rechenberg B, Darwiche S, Dailey HL. 2021. Virtual mechanical tests out-perform morphometric measures for assessment of mechanical stability of fracture healing in vivo. J Orthop Res [Internet]. 39(4):727–738.

https://doi.org/10.1002/jor.24866

Schwarzenberg P, Maher MM, Harty JA, Dailey HL. 2019. Virtual structural analysis of tibial fracture healing from low-dose clinical CT scans. J Biomech [Internet]. 83(xxxx):49–56. https://doi.org/10.1016/j.jbiomech.2018.11.020

Simon U, Augat P, Utz M, Claes L. 2011. A numerical model of the fracture healing process that describes tissue development and revascularisation. Comput Methods Biomech Biomed Engin. 14(1):79–93. https://doi.org/10.1080/10255842.2010.499865

Taddei F, Pancanti A, Viceconti M. 2004. An improved method for the automatic mapping of computed tomography numbers onto finite element models. Med Eng Phys. 26(1):61–69. https://doi.org/10.1016/S1350-4533(03)00138-3

Viceconti M, Bellingeri L, Cristofolini L, Toni A. 1998. A comparative study on different methods of automatic mesh generation of human femurs. Med Eng Phys. 20(1):1–10. https://doi.org/10.1016/S1350-4533(97)00049-0

Wirtz DC, Schiffers N, Forst R, Pandorf T, Weichert D, Radermacher K. 2000. Critical evaluation of known bone material properties to realize anisotropic FE-simulation of the proximal femur. J Biomech. 33(10):1325–1330. https://doi.org/10.1016/S0021-9290(00)00069-5

Table 1: Virtual torsional rigidity results for representative combinations of material assignment slope and soft tissue cutoff. Combinations with an asterisk denote the optimal design points.

Datum Reference: Biomechanical Testing	Group		Biomechanical Rigidity, GJ	Validation Criteria		
	Intact Ovine Tibiae (N=20)		$1.180 \pm 0.187 \text{ N-} \\ \text{mm}^{2/\circ}$	RMSE < Datum SD 0.187		
Finite Element Type	Slope [MPa- cm³/mgHA]	Cutoff [mgHA/cm3]	Torsional Rigidity, VTR [N-mm ² /°]	RMSE between VTR and GJ	Pearson's Correlations for VTR vs. GJ	
			[1 (11111 /]		\mathbb{R}^2	Significance
Tet-10	5,000	0	0.572 ± 0.092	0.619	0.699	p < 0.005
	11,250*	750*	1.182 ± 0.192	0.104	0.709	p < 0.005
	11,250	1,300	0.056 ± 0.025	1.136	0.328	p = 0.008
	20,000	1,500	0.005 ± 0.001	1.189	0.671	p < 0.005
Hex-8	5,000	0	0.560 ± 0.101	0.630	0.743	p < 0.005
	11,250*	1,050*	1.158 ± 0.205	0.101	0.759	p < 0.005
	11,250	1,300	0.134 ± 0.056	1.057	0.411	p = 0.002
	20,000	1,500	0.005 ± 0.001	1.189	0.726	p < 0.005
Hex-20	5,000	0	0.557 ± 0.090	0.634	0.692	p < 0.005
	12,500*	1,100*	1.200 ± 0.183	0.099	0.729	p < 0.005
	12,500	1,300	0.112 ± 0.046	1.080	0.284	p = 0.016
	20,000	1,500	0.005 ± 0.001	1.189	0.674	p < 0.005

 Table 2: Mesh convergence results and mesh metrics for a representative sample in the dataset.

Group	Tet-10 Tetra Elen		Hex-8 Hexahedral Mesh Elements				
•	Representative Contralateral Tibia						
Mesh Metric	Nodes	Elements	Nodes	Elements			
2mm Surf. 2mm Vol.	232,651	155,963	7,709	4,827			
1.5mm Surf. 1.5mm Vol.	512,425	358,439	16,772	11,396			
1.2mm Surf. 1.2mm Vol.	985,208	701,964	30,546	22,181			
1mm Surf. 1mm Vol.	1,695,785	1,222,176	50,192	38,079			
0.8mm Surf 0.8mm Vol.	3,301,479	2,405,701	92,824	73,940			
0.6 mm Surf. 0.6 mm Vol.	7,802,860	5,745,910	210,080	176,201			
0.4mm Surf. 0.4mm Vol.	Failed	Failed	671,646	595,125			
0.2mm Surf. 0.2mm Vol.	Failed	Failed	5,110,526	4,793,927			
0.1mm Surf. 0.1mm Vol.	Failed	Failed	39,225,834	37,830,643			

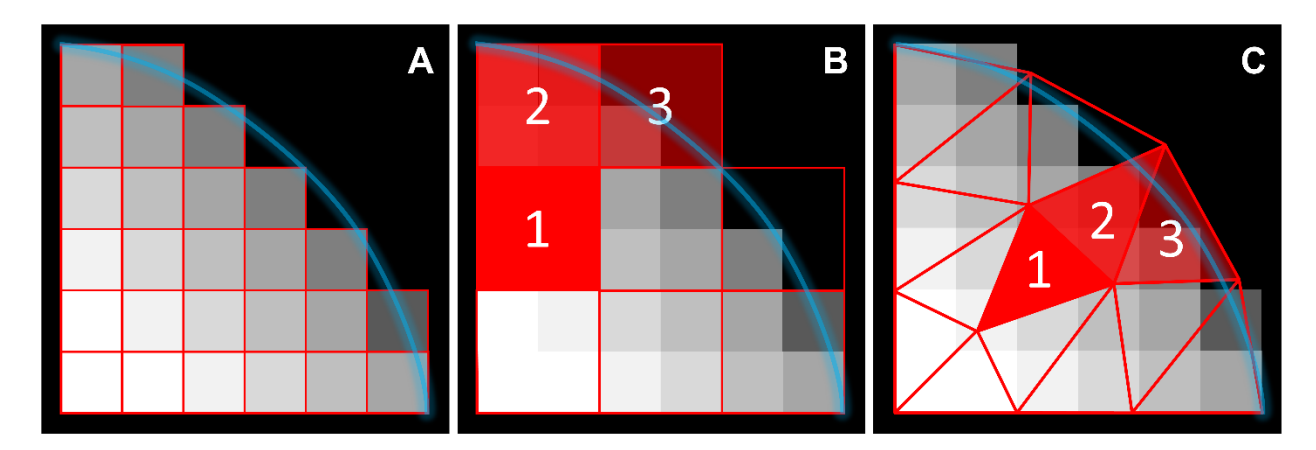


Figure 1: Partial volume effects in model reconstruction depend on the element type: (A) A hexahedral mesh of the same resolution as the underlying scan has partial volumes from image acquisition, but not from model reconstruction. Elemental properties are computed using the gray value for each voxel. (B) Increasing the hexahedral mesh size increases partial-volume blur and geometric inaccuracy at tissue boundaries. Representative elements 1, 2, and 3 have properties averaged from the underlying voxels. (C) A tetrahedral mesh follows the physiologic contour of the bone geometry, but is still susceptible to partial volume effects from model reconstruction.

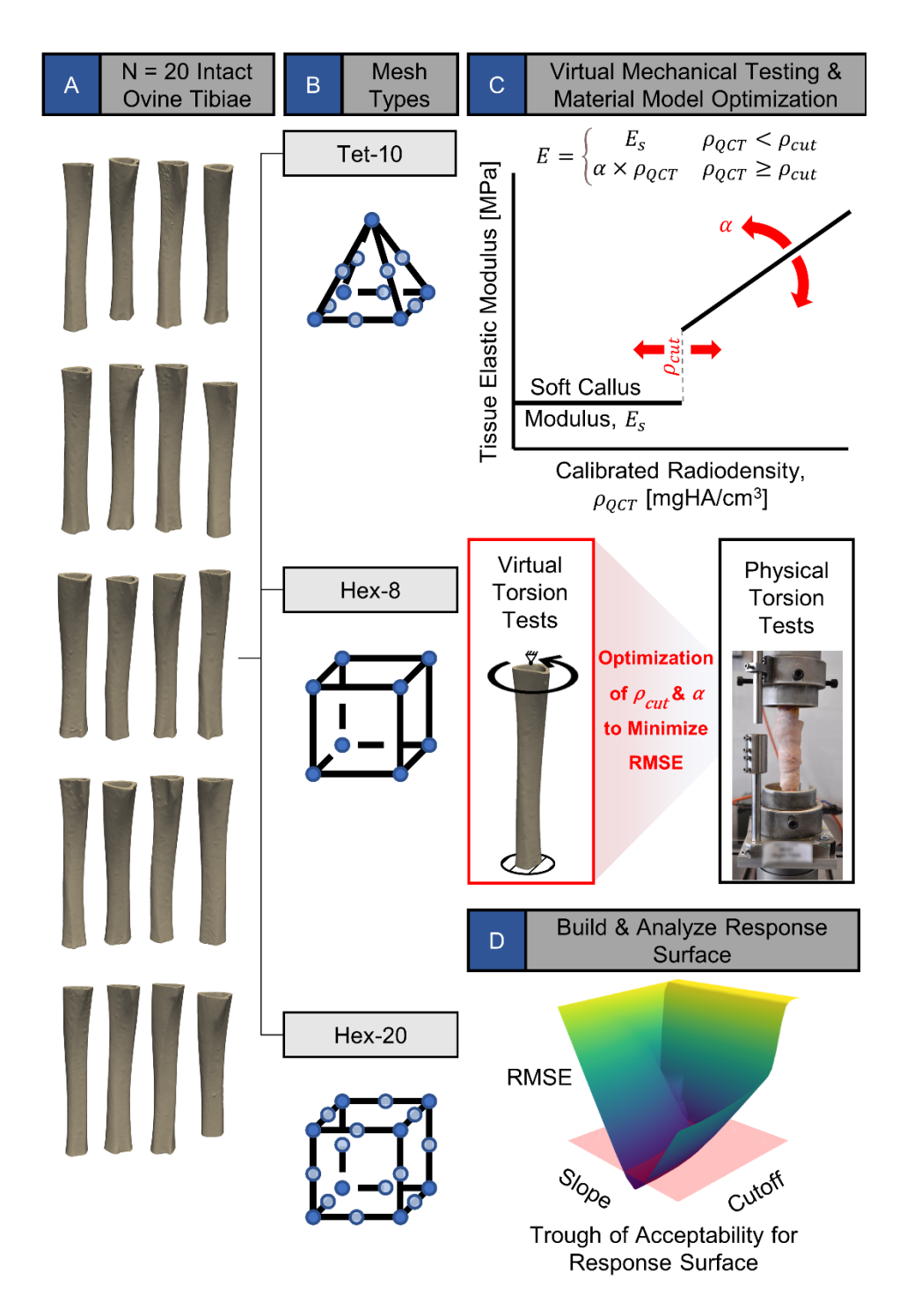


Figure 2: Overview of study design. (A) The ovine dataset included N = 20 intact tibiae. (B) All models were meshed using three element types. (C) The dual-zone material assignment law was used to manage partial volume effects when converting local radiodensity to tissue elastic modulus. The slope (α) and the soft tissue cutoff (ρ_{cut}) were systematically varied to minimize the RMSE between the virtual and physical torsion tests. (D) Response surfaces were created for each element type to identify combinations of slope and cutoff that reduced RMSE below the pre-defined acceptance limit for model validity.

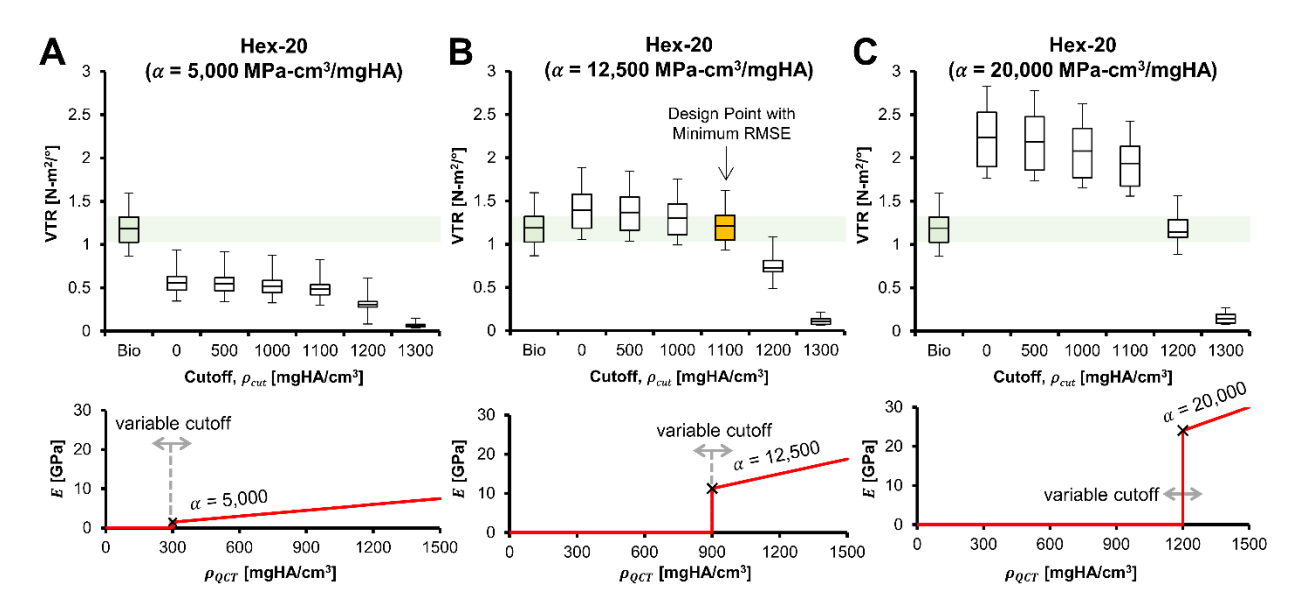


Figure 3: Representative results of dual-zone material model optimization for the Hex-20 element type. In each panel, the green "Bio" group is the target for optimization: GJ values from postmortem biomechanical testing. From left to right, panels (A) (B) and (C) show the effect of increasing density-modulus slope values α in the piecewise material model. The top row shows the effect of sweeping the density cutoff from low to high on predicted whole-bone rigidity. When the slope value is too low (panel A), all virtual models under-predict rigidity. When the slope value is too high, the virtual models tend to over-predict rigidity. The design point yielding the minimum RMSE is shown in gold in panel (B). The Hex-8 and Tet-10 models displayed similar behavior (see Supplemental Digital Content).

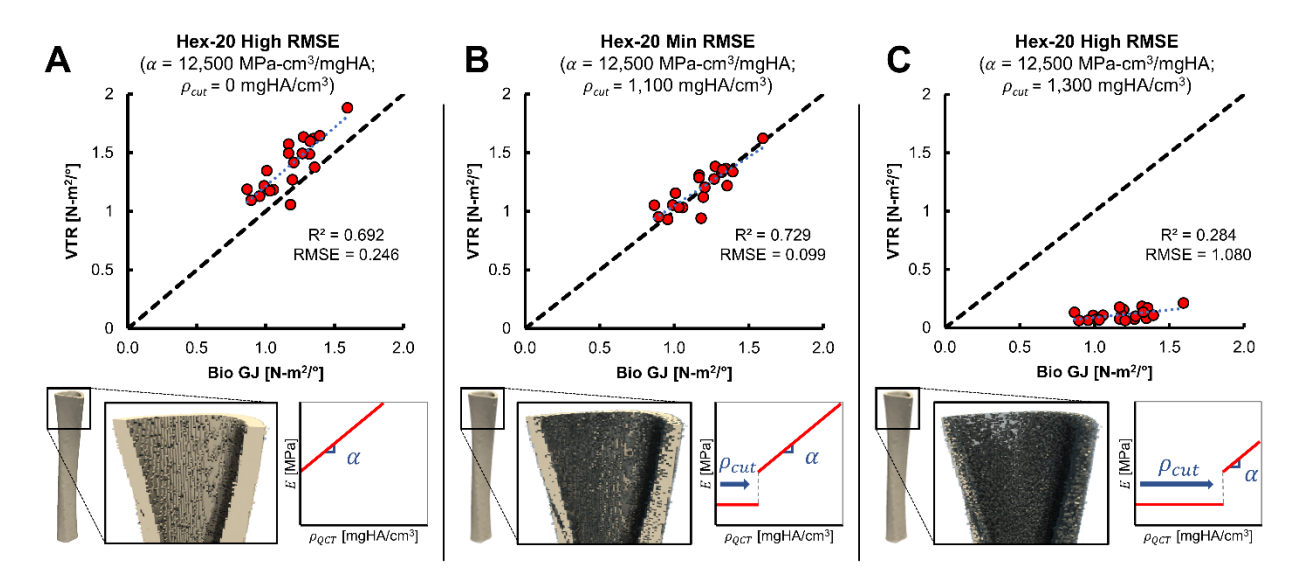


Figure 4: Effect of density cutoff on finite element model performance for representative Hex-20 element type. (A) The zero-cutoff case with no partial volume management produced a small but systematic over-prediction of torsional rigidity (VTR) compared to postmortem biomechanical testing (GJ). (B) At the optimal design point, the dual-zone material model achieved strong correlation between VTR and GJ with good absolute agreement. (C) At cutoffs above the optimal design point, VTR deteriorated to low values and cortical bone elements were incorrectly assigned properties for soft tissue. The 3D models shown in the bottom row illustrate how partial volume management is achieved via the dual-zone material model, with dark blue elements below the density cutoff being modeled as soft tissue. The Hex-8 and Tet-10 models displayed similar behavior (see Supplemental Digital Content).

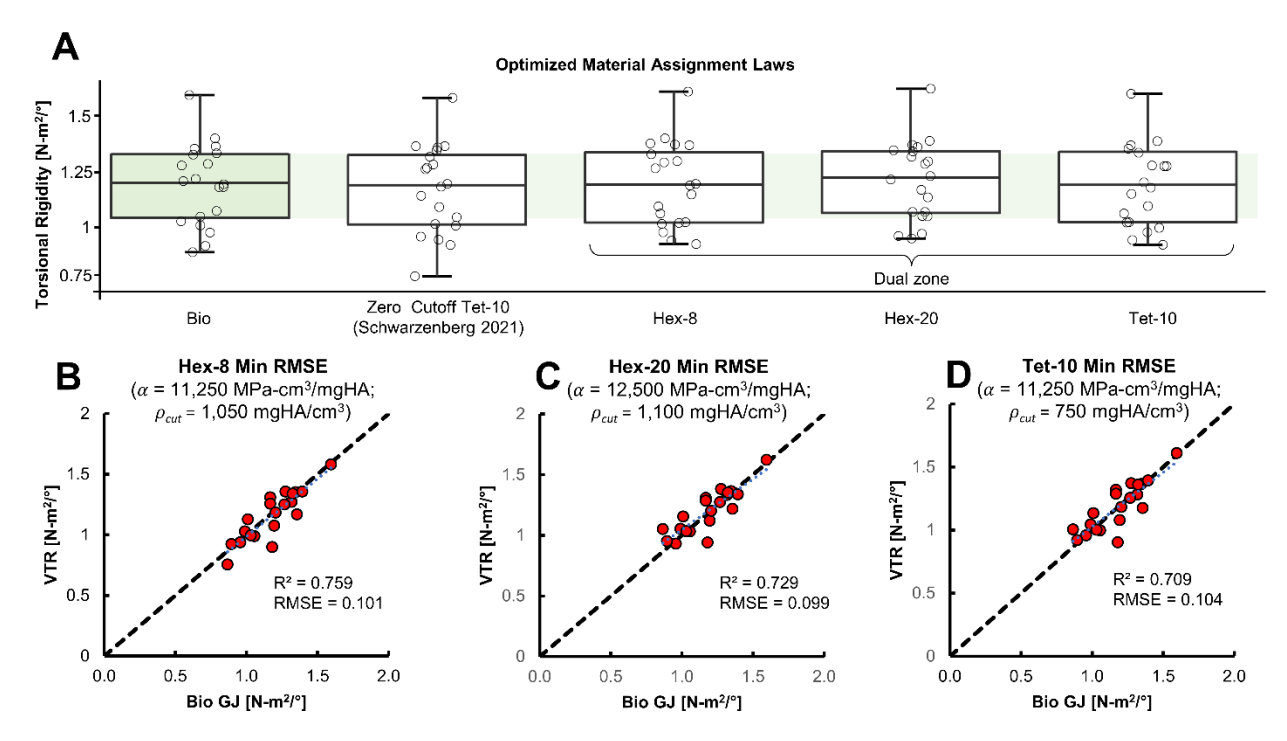


Figure 5: (A) All three element types achieved good agreement between VTR and GJ with the dual-zone material model. (B/C/D) For all element types, the correlations between VTR and GJ were strong and the RMSE values were below the datum (GJ) standard deviation, indicating that the finite element models are a reliable surrogate for the physical biomechanical tests.

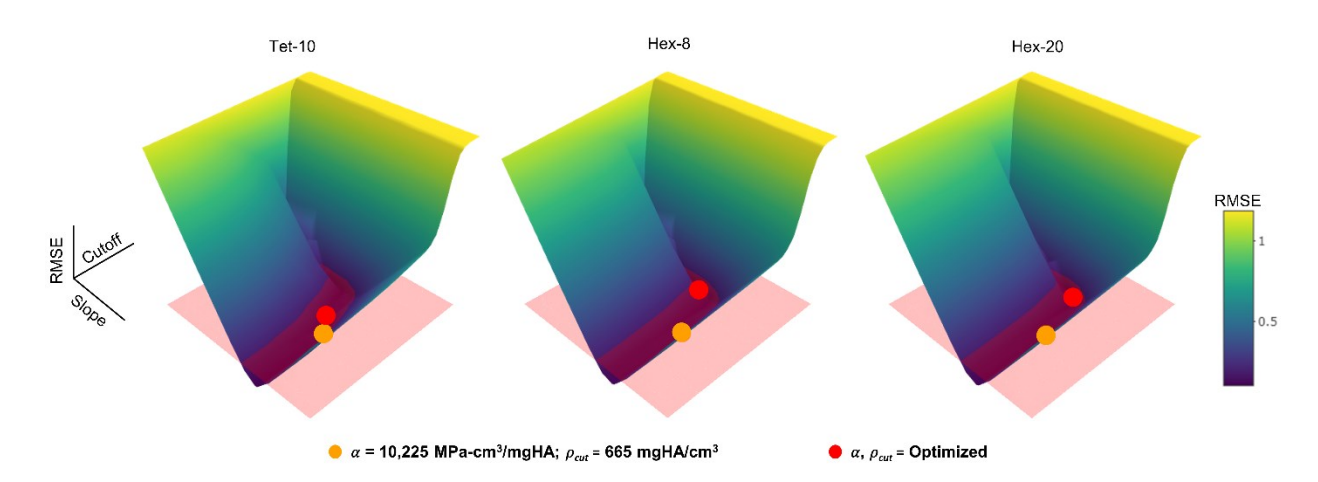


Figure 6: Response surfaces for all three element types show that there are a range of combinations slope and cutoff in the dual-zone material model that achieve acceptable agreement between VTR and GJ. The RMSE < datum SD criterion is visualized as a red plane. The "trough of acceptability" for the response surface dips below the red plane and represents the range of α and ρ_{cut} values that can be used together to mitigate partial-volume effects in these models and meet the pre-defined validity requirement. Orange dots correspond to our recommended implementation of the dual-zone approach to partial volume management for any element type; red dots are the locations of the absolute minimum RMSE values for each element type individually.